# Moist Convective Scaling: Some Inferences from Three-Dimensional Cloud Ensemble Simulations

FRANÇOISE R. ROBE AND KERRY A. EMANUEL

*Center for Meteorology and Physical Oceanography, Massachusetts Institute of Technology, Cambridge, Massachusetts*

(Manuscript received 7 August 1995, in final form 15 April 1996)

ABSTRACT

Numerical simulations of the tropical atmosphere were performed using a three-dimensional, convection-resolving, nonhydrostatic cloud model, in order to characterize the sensitivity of mesoscale tropical convection to radiative forcing. The system is run into a state of statistical equilibrium for a range of imposed tropospheric radiative cooling rates.

The heat budget implies that there should be a larger cloud mass flux for increasing radiative cooling; it does not exclude the possibility of more intense updrafts, but does not require it. In the numerical simulations, it is found that the increase of cloud areal coverage accounts for all the increase of the cloud mass flux required to balance an increase of the radiative cooling rate. At equilibrium, the mean updraft velocity in the clouds is independent of the magnitude of the radiative forcing.

## 1. Introduction

The concept of statistical energy equilibrium of moist convection (quasi-equilibrium) was first introduced by Arakawa and Schubert (1974), who argued that the timescale by which turbulent kinetic energy of moist convection adjusts to changes in the large-scale forcing is small compared to that over which the forcing evolves. Observational evidence supporting the basic concept of quasi-equilibrium was presented by Arakawa and Schubert and, more recently, by Wang and Randall (1994), who showed that although oscillations in convective available potential energy (CAPE) on timescales less than about three days were not entirely negligible, the quasi-equilibrium hypothesis was well verified.

Raymond (1995a) pointed out that the principal way in which deep convection stabilizes the atmosphere is by transporting midlevel, low-entropy air into the subcloud layer in precipitation-driven downdrafts and he proposed a form of quasi-equilibrium based on entropy equilibrium of the subcloud layer. This closure works well in a numerical model of tropical cyclone development (Emanuel 1995).

While quasi-equilibrium has been successful in relating convective mass fluxes to large-scale forcing, it leaves unresolved the question of convective velocity and buoyancy scales, as well as the issue of fractional areal coverage of convective clouds [Emanuel et al. (1994); the convective mass flux is the product of a velocity scale and a fractional area scale; knowledge of the mass flux by itself is insufficient for determining the velocity and fractional area scales individually]. This problem is unique to moist convection; velocity scales for dry convecting boundary layers are well known (Prandtl 1925; Deardorff 1972).

The issue of moist convective scaling is also closely related to the problem of determining the connection between moist convective plumes and boundary layer convection. Betts (1982) and Xu and Emanuel (1989) argued that those parts of the tropical atmosphere experiencing deep convection are nearly neutral to upward displacements of air from near the top of the subcloud layer, implying that updraft air originates in the surface layer, which has considerably higher entropy [the neutrality of the deep troposphere to mixed-layer displacement was later questioned by Williams and Renno (1993)]. These studies support earlier deductions about the level of origin of air ascending within tropical cumulonimbi (e.g., Zipser and LeMone 1980; Renno and Williams 1995). Recent work by Raymond (1995b), using TOGA COARE data, also suggests that moist convection originates at low levels within the subcloud layer. Determining the correct scales for moist convective velocities, buoyancies, and areal coverage may also help rationalize observations in deep tropical regimes. Comparing theoretical values of CAPE to values calculated by lifting parcels from different levels in real soundings may help identify the origin level of air participating in deep convection.

These issues motivated a series of numerical experiments aimed at empirically determining dependencies of moist convective velocity and buoyancy scales on

*Corresponding author address:* Dr. Françoise R. Robe, Center for Meteorology and Physical Oceanography, MIT, Room 54-1611, 77 Massachusetts Ave., Cambridge, MA 01239.
E-mail: robe@squall.mit.edu

the magnitude and distribution of imposed large-scale forcing and to undertake a theoretical explanation of the results observed in the numerical simulations. In this paper we describe the results of simulations using a fully nonhydrostatic cloud model integrated over a domain large enough to contain many clouds and long enough to attain statistical equilibrium. In a companion paper, Emanuel and Bister (1996) describe simulations using a radiative-convective model and develop a theory for moist convective scales.

In section 2 of this paper, we describe the nonhydrostatic model used in the experiments, the boundary and initial conditions imposed, and the forcing. Section 3 describes the results of the simulations, and section 4 presents concluding remarks.

## 2. Numerical experiments

Our motivation here is to use a reasonably complete model to obtain realistic simulations of a tropical cloud field in statistical equilibrium and to extract a few key data, averaged over space and time, in order to characterize the equilibrium state and answer a few simple questions. How do the mean thermodynamic sounding and the lapse rate vary as a function of the radiative forcing? How does CAPE vary? How is the enhanced cloud mass flux shared between clouds? Does the areal coverage of clouds increase and/or do the updrafts intensify with increased forcing?

We employ the ARPS model version 3 (Xue et al. 1993), a three-dimensional, nonhydrostatic cloud model that explicitly resolves convection. The warm rain processes are parameterized after Kessler (1969; there is no ice in the model). We add a constant radiative cooling, $R$, from the surface to 13 km. Above 14 km, Newtonian heating relaxes the temperature to observed tropopause and stratosphere profiles (Jordan 1958); this effectively imposes a nearly constant tropopause altitude. Water conservation is enforced, which is vital for reaching equilibrium. Most cloud models simply set negative mixing ratios to zero, effectively adding water to the system continuously. In our simulations, we bring negative mixing ratios to zero by redistributing water from neighboring points, in an amount proportional to what is available at each of these points. This procedure eliminates negative mixing ratios while conserving water in the whole system. The lower boundary is a passive ocean with a fixed surface temperature (300 K). A minimum wind speed of 10 m $s^{-1}$ is added to the actual wind for the computation of the surface fluxes of heat and moisture only, using the bulk aerodynamic formula with a drag coefficient of $10^{-3}$. This minimum wind speed is somewhat larger than commonly observed over tropical oceans. We use this large value partly to account for the effects of a mean wind, which is absent in our model, and partly to accelerate the approach to equilibrium and thereby reduce computational expense. Since the equilibrium enthalpy flux is dictated by the imposed radiative cooling rate of the atmosphere, it is not affected by the chosen surface wind speed, and the use of a large value only slightly affects the mean surface air temperature and humidity. There is no surface flux of momentum and no planetary rotation.

The domain is doubly periodic and therefore effectively infinite in both horizontal directions. This is important for reaching equilibrium since inflow from outside the domain would bring in air that is not in equilibrium. A sponge layer extends from 15.5 km to 19 km, with a relaxation time of 100 s. The momentum sponge layer begins somewhat higher than the thermodynamic sponge layer (14 km) in order to let clouds naturally overshoot their levels of neutral buoyancy. The domain extends over a 60-km by 60-km area, which is a small but suitable dimension for our purpose. Experiments with a domain that is four times as large but with the same resolution lead to the same qualitative and quantitative results when averaged over time; the time series are smoother when horizontally averaged over a larger domain, but this is of importance only if one wishes each instantaneous snapshot to be representative of the whole picture.

The initial atmosphere is horizontally homogeneous with a vertical structure similar to Jordan's sounding (1958) for the hurricane season in the West Indies (the choice of an initial sounding should not affect the equilibrium state). The system is destabilized by constant radiative cooling from the surface to the tropopause. Six cases will be discussed here for a large range of cooling rates: 1.07, 1.43, 2.14, 4.28, 5.35, and 6.42 K $day^{-1}$; we will denote them R11, R14, R21, R43, R54, and R64, respectively. The convection is initiated with spatially random surface air temperature perturbations maintained for 30 min. The perturbations range from −0.2°C to 0.2°C but produce no domain-averaged heating. Convective clouds start to develop over the entire domain and after a few days the system reaches statistical equilibrium.

Careful examination of the model variables shows that there are at least two different timescales over which the system reaches equilibrium. The precipitation and virtual temperature profile reach equilibria in a matter of days, reflecting the natural timescale for buoyancy adjustment. The water vapor profile takes much longer to reach equilibrium, reflecting the long timescale (~30 days) of subsidence outside of clouds. As we are interested in the equilibrium buoyancy and velocity scales, however, it is not necessary (and prohibitively expensive) to allow the water vapor profile to reach perfect equilibrium.

The experiments described here are similar to those performed by Islam et al. (1993), who used another nonhydrostatic model run in both two and three dimensions. Their results show that two-dimensional simulations require extremely large domains to achieve the same degree of statistical stability as three-dimensional simulations, owing to the strong preference of moist convection for three-dimensional geometry (e.g.,

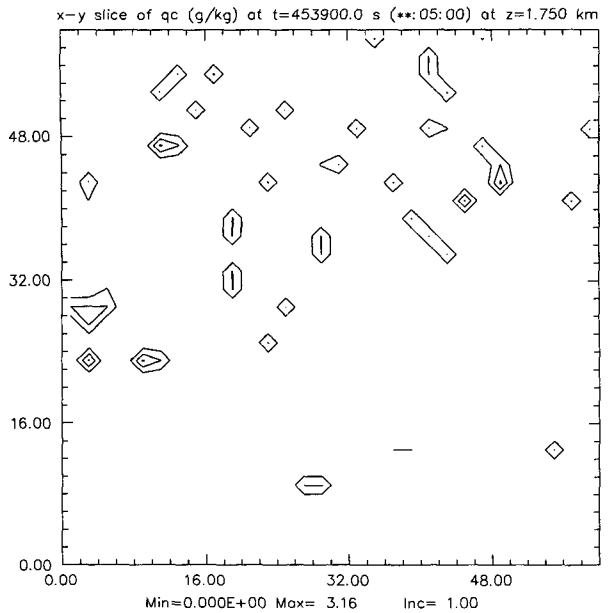


a) Cloud: horizontal cross-section (XY) at z=1.75 km

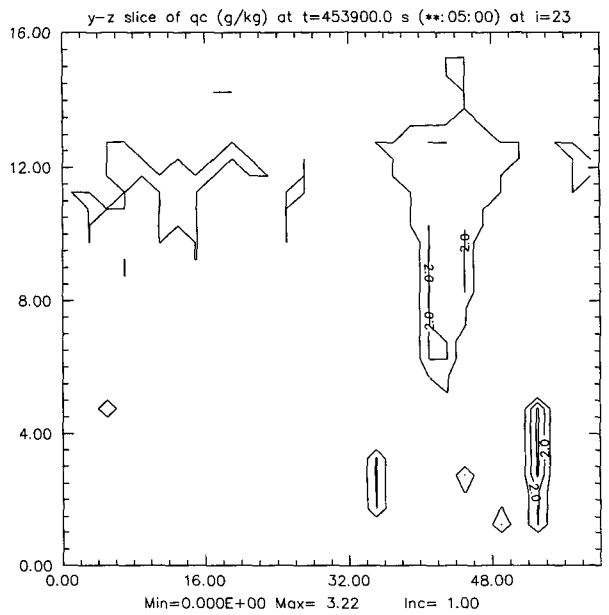


b) Cloud: vertical cross-section (YZ) at x= 43km

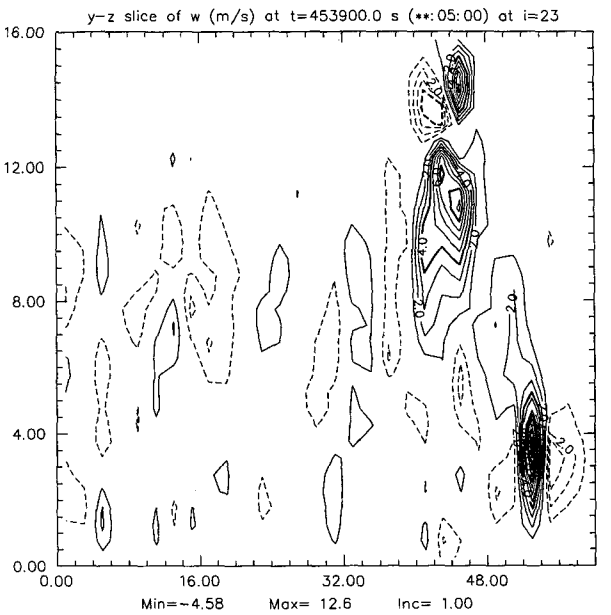


c) Vertical velocity: vertical cross-section (YZ) at x= 43km

FIG. 1. Cloud field after 126 h for $R = -5.4$ K day$^{-1}$: (a) horizontal cross section ($XY$) of the cloud water content ($Q_c$) at $z = 1.75$ km, (b) vertical cross section ($YZ$) of $Q_c$ at $x = 43$ km, and (c) vertical cross section ($YZ$) of the vertical velocity field ($w$) at $x = 43$ km. The units for $Q_c$ are such that for $q_c < 0.01$ g kg$^{-1}$: $0 < Q_c < 1$; $0.01 < q_c < 0.1$: $1 < Q_c < 2$; $0.1 < q_c < 1$: $2 < Q_c < 3$; and $1 < q_c < 10$: $3 < Q_c < 4$.

see Lilly 1960) and, possibly, to the necessity for energy to cascade to larger scale in two dimensions. We therefore question the usefulness of two-dimensional simulations of ensemble convection. Tao et al. (1987) did note similarities between their two- and three-dimensional cloud ensemble simulations, but the convection in the three-dimensional simulations was biased toward two-dimensional structure by a combination of imposed vertical wind shear and maintained two-dimensional temperature perturbations. Moreover, the simulations were run for only 6 h and could not reach statistical equilibrium. We believe that, at least in the unsheared case, three-dimensional simulations are necessary for qualifying the properties of moist convection in statistical equilibrium with forcing.

The system reaches a statistical equilibrium, where clouds grow and die, and not a fixed state. Figure 1a shows an instantaneous horizontal cross section of the cloud field at an altitude of 1.75 km for the R54 experiment after 126 h of integration. Figure 1b displays a vertical cross section through the cloud field at the same time and shows clouds at various stages of their

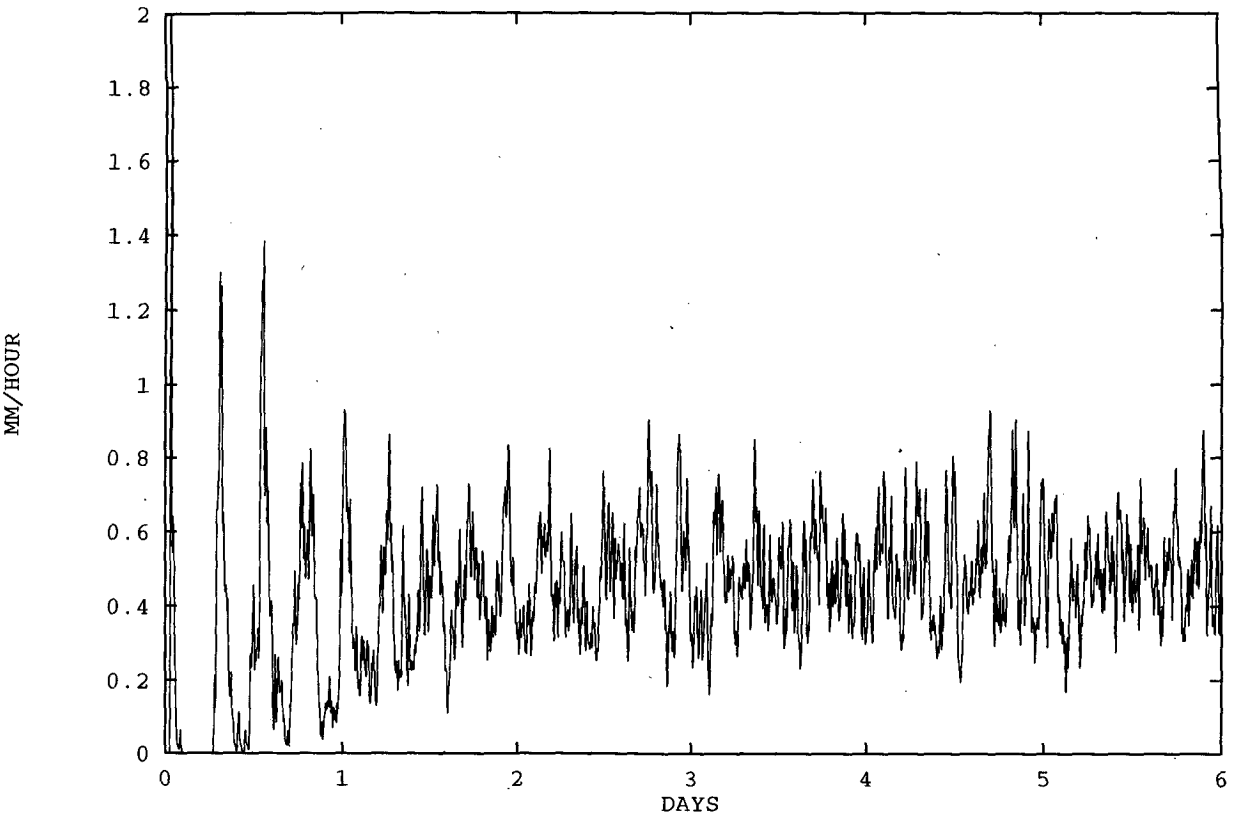


FIG. 2. Time series of the horizontally averaged rainfall rate at the ground for R54.

life. From right to left one can observe a young cumulonimbus rising from the surface to about 5 km, a mature cloud reaching the tropopause, and a decaying anvil. The corresponding vertical velocity field (Fig. 1c) shows the associated updrafts and downdrafts; the latter are located under and next to the clouds, owing to rain falling into unsaturated air. Owing to the high frequency variability of the system, instantaneous snapshots may be unrepresentative. At equilibrium, running one-day window averages of the rainfall vary by as much as 20%. Precipitation is, by far, the most variable quantity in the system, leading us to choose two days as an averaging period; this reduces the variability of rainfall to 7%. The variability of all the other variables is at least an order of magnitude smaller. All the variables are averaged over two days, except for certain quantities that are averaged over 12-h periods.

## 3. Results

### a. Precipitation time series

As noted above, the system reaches statistical equilibrium after a few days of integration. The cloud distribution varies with time but the global cloud cover, the rainfall rate, the cloud mass flux, and the horizontally averaged thermodynamic sounding have little time tendency (except for the water vapor field, as noted previously). The spinup time depends on the radiative cooling rate: the stronger the radiative forcing, the faster the system reaches equilibrium. Equilibrium is reached in about 8 days for R11, while it takes only 4 days in the case of R64. This spinup process is best illustrated by the time series of horizontally averaged rainfall rate at the ground. Figure 2 shows the time series of the rainfall rate averaged over the whole area, denoted $R_f$, for R54. Initially, peaks of rain alternate with dry periods, then the rainfall, averaged over the domain, takes on a more continuous character. The dry/wet pattern never quite ends for the R11 experiment, but the running-1-day window time average of $R_f$ does stabilize, as do the mean thermodynamic sounding and the other properties, except for the relative humidity that still shows a small tendency for the smaller $R$ values.

### b. Temperature and humidity

At equilibrium, the horizontally averaged thermodynamic sounding varies little with time: the averaged surface temperature, which is the most variable horizontally averaged thermodynamic quantity, is constant with time within a few tenths of a degree. The horizontally averaged thermodynamic soundings for R11 and R54 are shown in Figs. 3a and 3b. The atmosphere is colder for larger radiative cooling rates $R$ and, since the height of the tropopause is practically fixed by imposing Newtonian re-

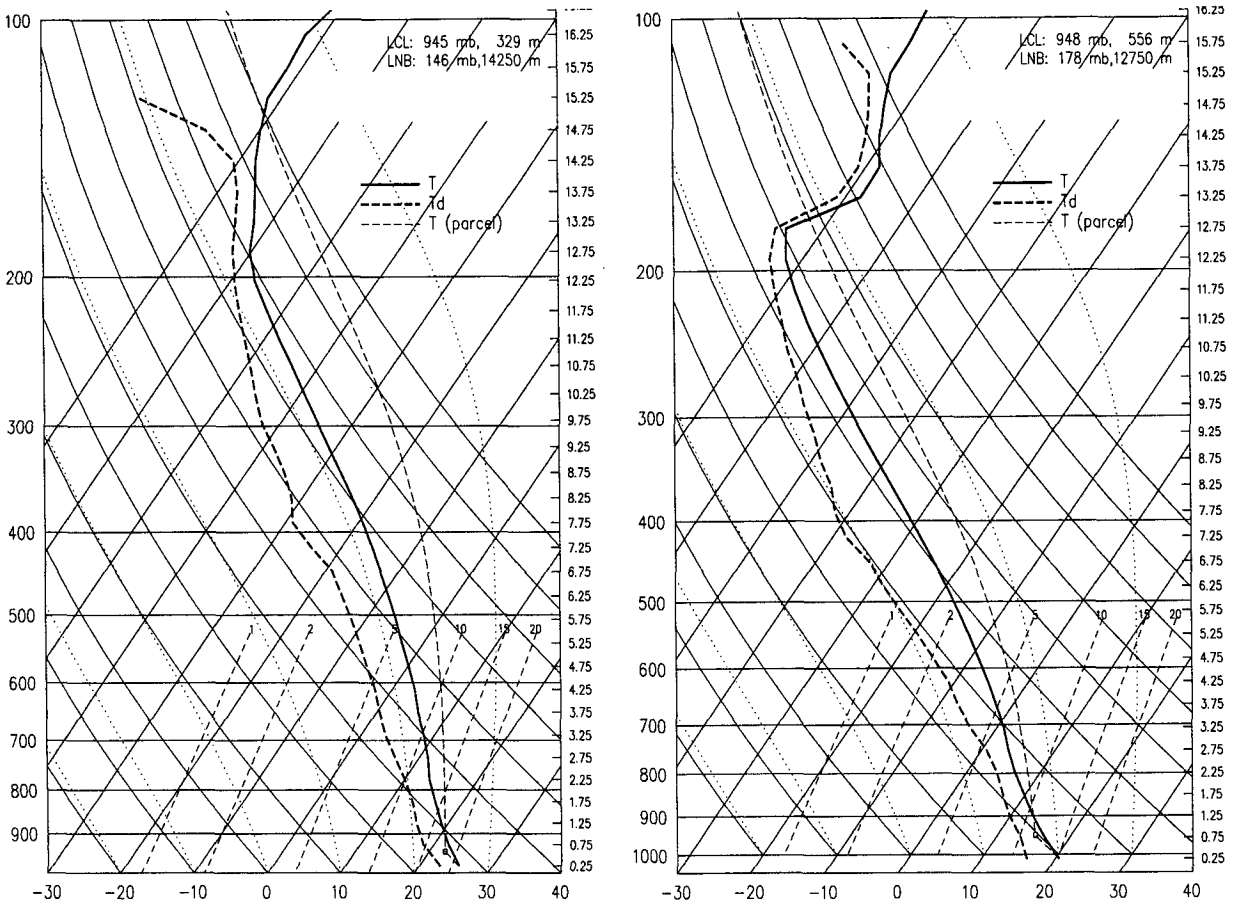


FIG. 3. Horizontally averaged thermodynamic sounding (a) for R11 and (b) for R54.

laxation above 14 km, a rather strong inversion develops between 13 and 14 km for the large $R$ experiments. Here, R11, R14, and R21, the closest to the present conditions in the Tropics, present a smooth decrease of temperature at that altitude. Without a detailed radiation model in the lower stratosphere, it is difficult to foresee the real shape of the tropopause. It would likely be smoother than what we obtain with the large cooling rates, and the altitude of the tropopause might be higher. The heat budget shows that there is an increasing source of heat in the sponge layer with increasing cooling rates. The tropospheric temperature decreases with increasing $R$, since to balance the increased radiative cooling, greater surface enthalpy fluxes are necessary. At fixed wind speed, this necessitates greater air–sea jumps of temperature and specific humidity and thus lower entropy of the surface air. When lifted moist adiabatically, this corresponds to lower air temperatures.

There is no qualitative change in the horizontally averaged vertical profile of the static stability, $d\theta_v/dz$, for the different experiments, as can be seen in Fig. 4. The stability $d\theta_v/dz$ is maximum around 3 km and near the tropopause and minimum around 11 km and close to the surface. The lapse rate decreases with increasing $R$. At all levels, the temperature decreases slightly more rapidly with height than a moist adiabat.

The horizontally averaged relative humidity is plotted as a function of altitude in Fig. 5 for R21 and R54. It amounts to about 80% in the lower troposphere, peaks slightly around 2.5 km, then decreases down to about 40% around 7.5 km, and increases again to over 85% near the tropopause. The position of the minimum at 7.5 km is consistent with climatological data (e.g., Sun and Lindzen 1993) as well as with data gathered during GATE (Reed et al. 1977). It does not depend very strongly on the radiative forcing. However, the larger the cooling rate, the drier the lower troposphere and the moister the upper troposphere. Unlike what is usually done in warm rain modeling, the autoconversion threshold decreases linearly from $10^{-3}$, its constant value above 0°C, to zero at and below −20°C. We did so to account for the observed precipitation from anvil clouds and to prevent saturation of the upper levels. Simulations performed with a fixed threshold show that the troposphere gets overly moist above 6 km, although the relative humidity profile still shows a well-defined minimum around 7.5 km.

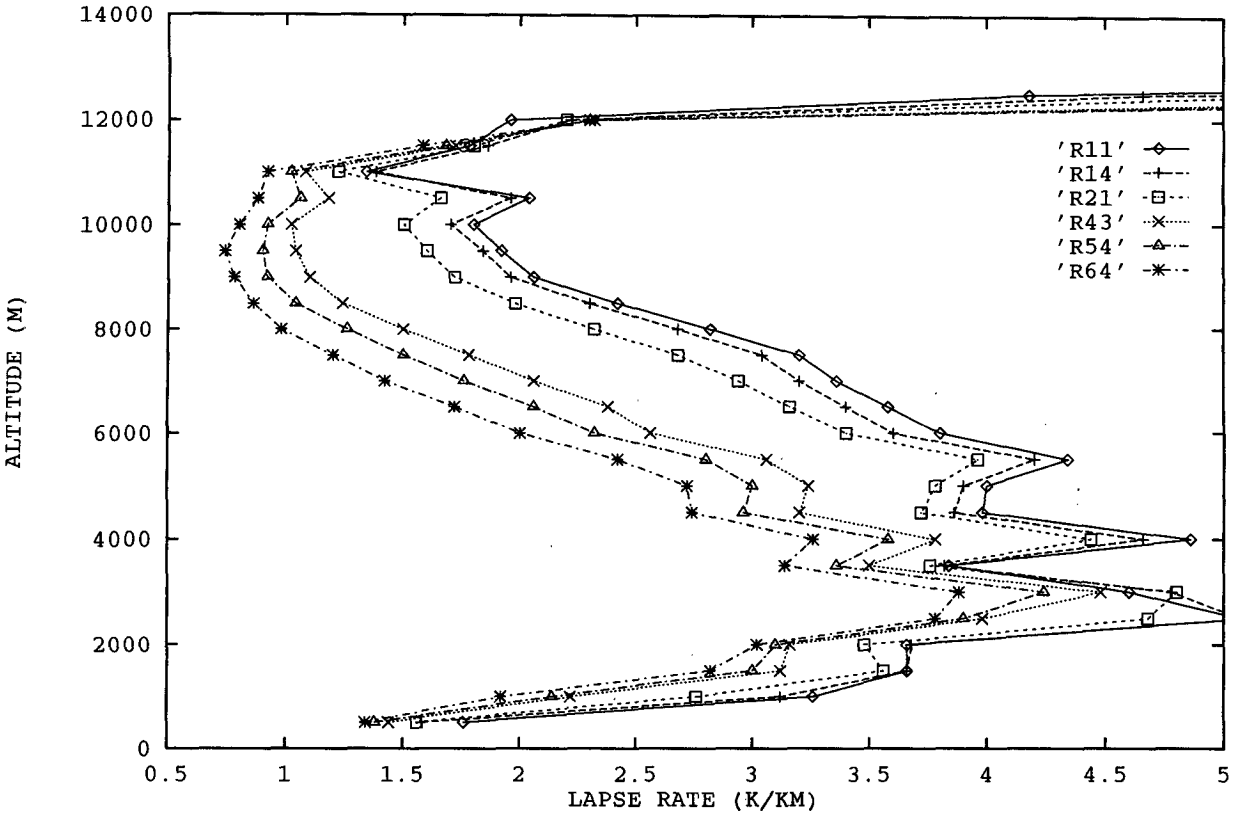


FIG. 4. Lapse rate $d\theta_v/dz$: horizontally averaged vertical profiles for R11, R14, R21, R43, R54, and R64.

*c. Upward mass flux*

At each level, we computed the upward cloud mass flux, defined as

$$M = \rho \sum_{q_c>0,w>0} \frac{A_c}{A} w_{i,j} = \rho \bar{w} \sigma, \qquad (1)$$

where $\rho$ is the air density, $A_c$ is the area covered by a single grid box, $A$ is the domain area, $q_c$ is the cloud water content, and $w_{i,j}$ is the vertical velocity at the horizontal grid point $i, j$. The quantity $\bar{w}$ is the upward vertical velocity averaged over all the cloudy points at a given level, and $\sigma$ is the fractional areal cloud coverage, defined, respectively, as

$$\bar{w} = \frac{1}{N_c} \sum_{q_c>0,w>0} w_{i,j}, \qquad (2)$$

$$\bar{\sigma} = \frac{N_c A_c}{A} \qquad (3)$$

where $N_c$ is the number of cloudy grid points at that level. Note that the summations in (1), (2), and (3) extend only over the cloudy points experiencing ascent. The saturated downdrafts are not included in the computation. The convective upward mass flux, $M_c$, and the corresponding mean convective velocity, $w_c$, and convective areal coverage, $\sigma_c$, are defined in the same way, but the summations extend only over the cloudy points where the vertical velocity is greater than 1 m s$^{-1}$, according to a widely used definition of convective updrafts (e.g., LeMone and Zipser 1980). Other criteria have been designed to define convective areas in cloud model simulations (e.g., Sui et al. 1994; Xu 1995); these are based not only on the updraft velocities but also on rainfall and cloud water content. They define convective columns, whereas we are specifically interested in updraft properties.

The time-averaged vertical profiles of the upward mass flux and the convective upward mass flux are shown in Fig. 6 for R21 and R54. The mass flux spectra exhibit two main peaks, one around 2 km, and another one around 10 km, similar to the bimodal mass flux distribution observed in the Tropics (e.g., Nitta 1975). The lower peak corresponds to low-level cumulus clouds, while the higher one corresponds to deep cumulonimbi. The deep clouds entrain surrounding air, as indicated by the increasing upward mass flux with height. The time-averaged upward mass flux appears more constant with height for low radiative cooling rates; this is not owing to the absence of entrainment but rather to time-varying cloud top altitudes and velocities.

Based on the shape of these vertical profiles, we choose 6.75 km as an appropriate altitude for charac-

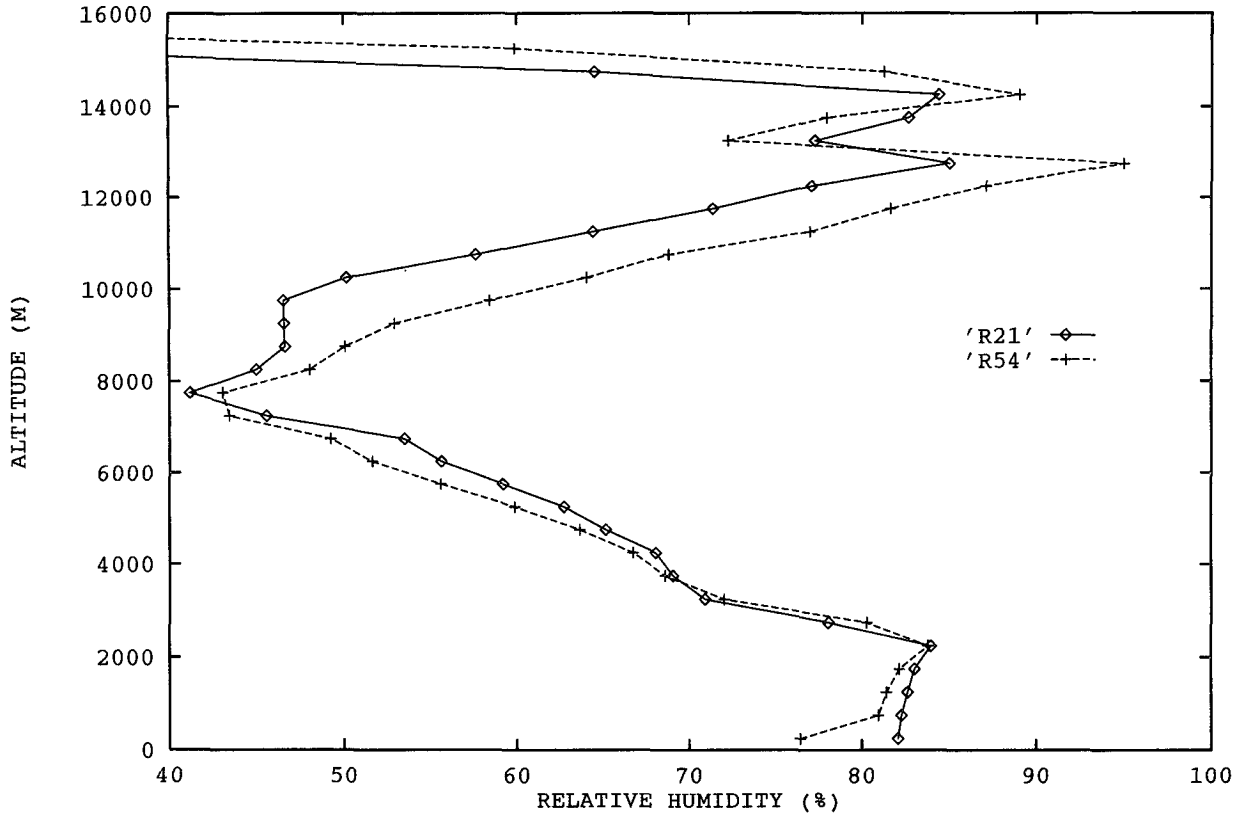


FIG. 5. Relative humidity: horizontally averaged vertical profiles for R21 and R54.

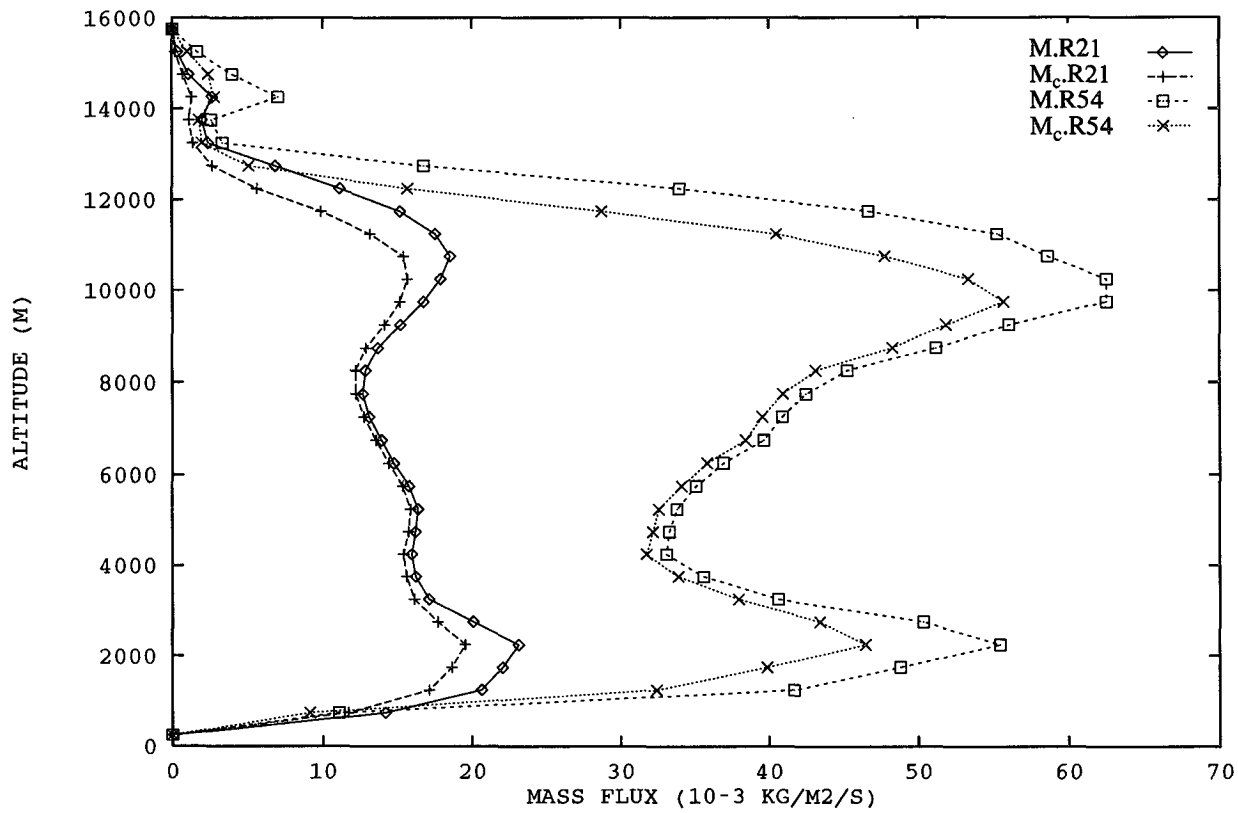


FIG. 6. Upward cloud mass flux: time-averaged vertical profiles for R21 and R54 for ascent ($M \cdot$R21, $M \cdot$R54) and for convective ascent ($M_c \cdot$R21, $M_c \cdot$R54).

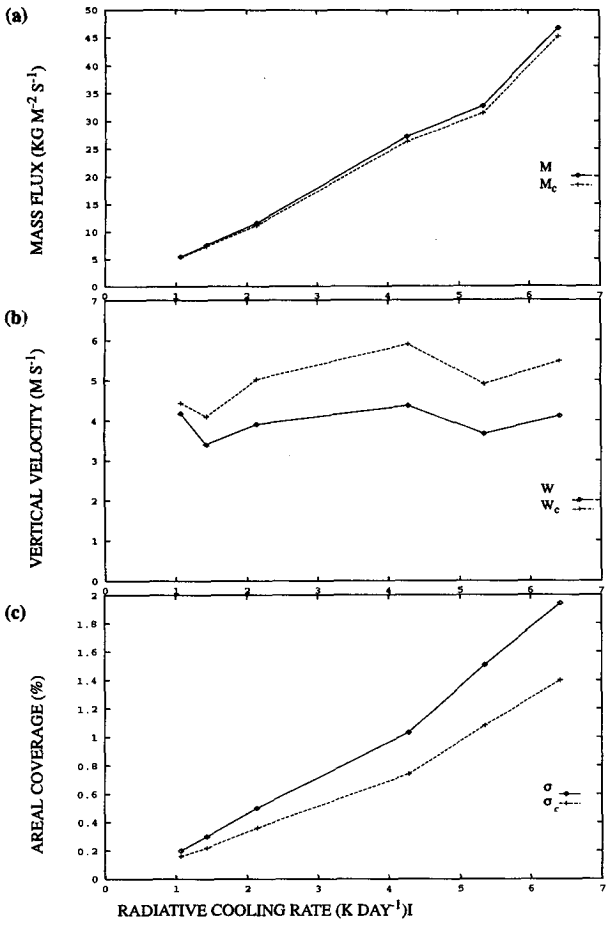


FIG. 7. Time mean of cloud properties at 6.75 km of altitude, plotted as a function of the cooling rate, $R$, and logarithmic curve fits. (a) Upward cloud mass flux $M$ and convective mass flux $M_c$. (b) Mean upward velocity $\bar{w}$ and mean convective velocity $\bar{w}_c$ in the clouds. (c) Areal coverage of cloudy updrafts $\sigma$ and of convective updrafts $\sigma_c$ (units are in percentages of the total area).

terizing the cumulonimbi: the vertical velocities are near their peak magnitudes and large entrainment has not yet commenced. The behavior of the velocities at this level is similar to that at other levels. The upward mass flux and convective mass flux at that altitude are shown in Fig. 7a as a function of the imposed radiative cooling rate $R$. The mass flux increases slightly more than linearly with $R$, reflecting the decreasing static stability associated with lower temperatures, since

$$\frac{M}{\rho}\frac{\partial\theta}{\partial z} \sim R\frac{\theta}{T},$$

although this neglects the downdraft mass flux. Logarithmic curve fits give

$$M \sim R^{1.17},$$
$$M_c \sim R^{1.16}.$$

*d. Convective velocities*

The mean upward velocity, $\bar{w}$, and convective upward velocity, $\bar{w}_c$, defined by (2), are shown in Fig. 8 as a function of altitude for R11 and R64. There is a clear peak at middle levels, but the velocities are practically independent of the magnitude of the cooling. Logarithmic curve fits for the vertical velocity at 6.75-km altitude (Fig. 7b) give

$$\bar{w} \sim R^{0.03},$$
$$\bar{w}_c \sim R^{0.14}.$$

The maximum vertical velocity over the entire domain is one estimate of the intensity of deep convection. It does not measure how the ensemble of clouds reacts to a variation of radiative cooling but how intense the convection can get in a particular area for a given cooling rate. Combined with a measure of the mean vertical velocity in the updrafts, it indicates how wide the updraft velocity spectrum is and whether this spectrum varies with $R$. It gives an upper bound on the convective velocity scale and a lower bound on the convective timescale. It is also directly related to the range of air surface entropies, since the higher the buoyancy of a surface parcel, the faster it ascends.

The time series of the maximum vertical velocity in the domain exhibits large high-frequency (minutes) variability but small low-frequency (hours) variability (not shown). The time mean, $w_{\max}$, increases with increasing $R$ by as much as 57% between R21 and R54. This increase of $w_{\max}$ with $R$ is consistent with the larger spatial variability of the surface layer entropies at high $R$.

*e. Areal coverage*

Vertical profiles of the time-mean fractional areal coverage of all updrafts, $\sigma$, and of convective updrafts, $\sigma_c$, defined by (3), are shown in Fig. 9 for R21 and R54. There are two peaks in the areal coverage of clouds: a low-level peak corresponding to shallow clouds and a peak near the tropopause corresponding to spreading stratiform anvils.

The density of deep convective cores increases more than linearly with $R$, varying approximately at $R^{1.2}$ (Fig. 7c). The clouds experiencing ascent at 6.75 km cover from 0.2% to 2% of the whole area, much less than the anvils near the tropopause, which cover from 12% to 65% of the domain. The ratio of the area covered by anvils to the area covered by convective cores at 6.75 km decreases with $R$. Some 72% of the cores at 6.75 km experience ascent greater than 1 m s$^{-1}$. This proportion slightly decreases between R11 and R21 but is virtually constant for higher $R$.

*f. Convective available potential energy*

The domain-averaged values of the convective available potential energy (CAPE) are shown in Fig. 10,

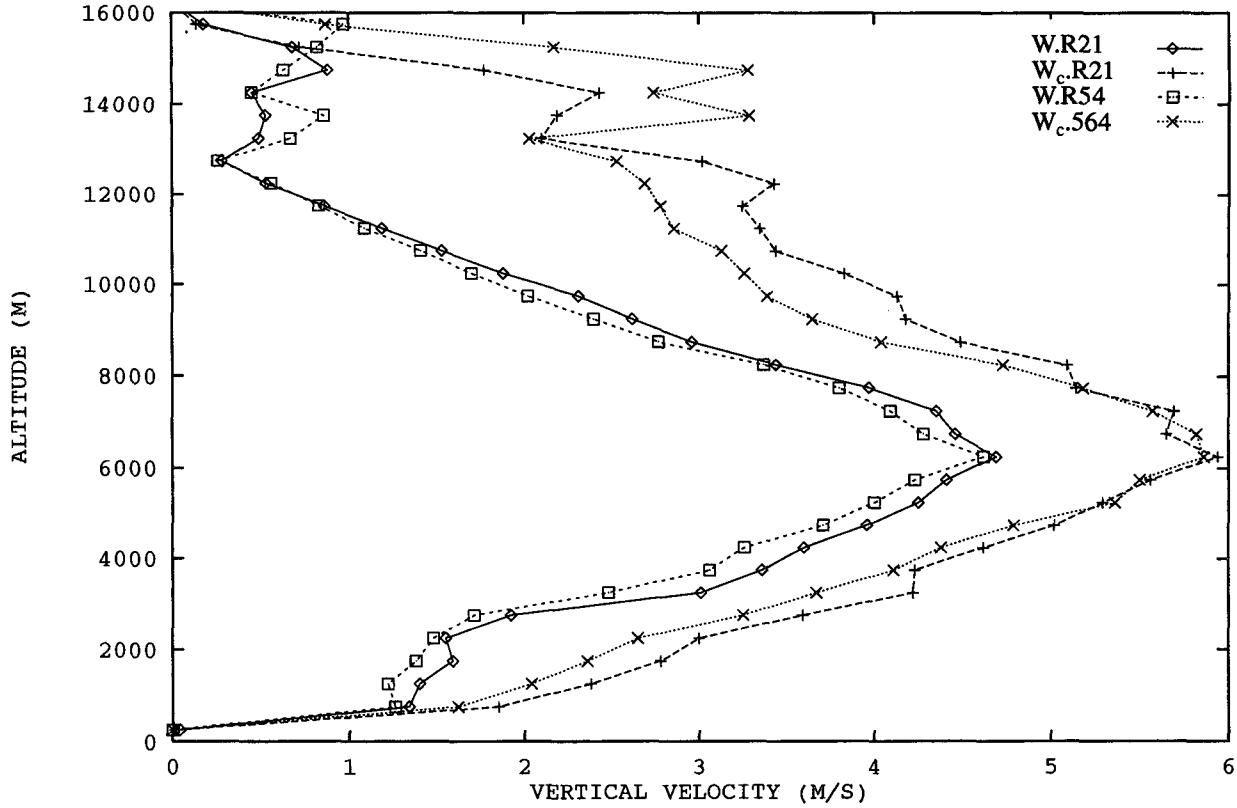


FIG. 8. Mean upward velocities in the clouds: time-averaged vertical profiles for R21 and R54 for clouds experiencing ascent $w \cdot$R21, $w \cdot$R54, and convective ascent $w_c \cdot$R21, $w_c \cdot$R54.

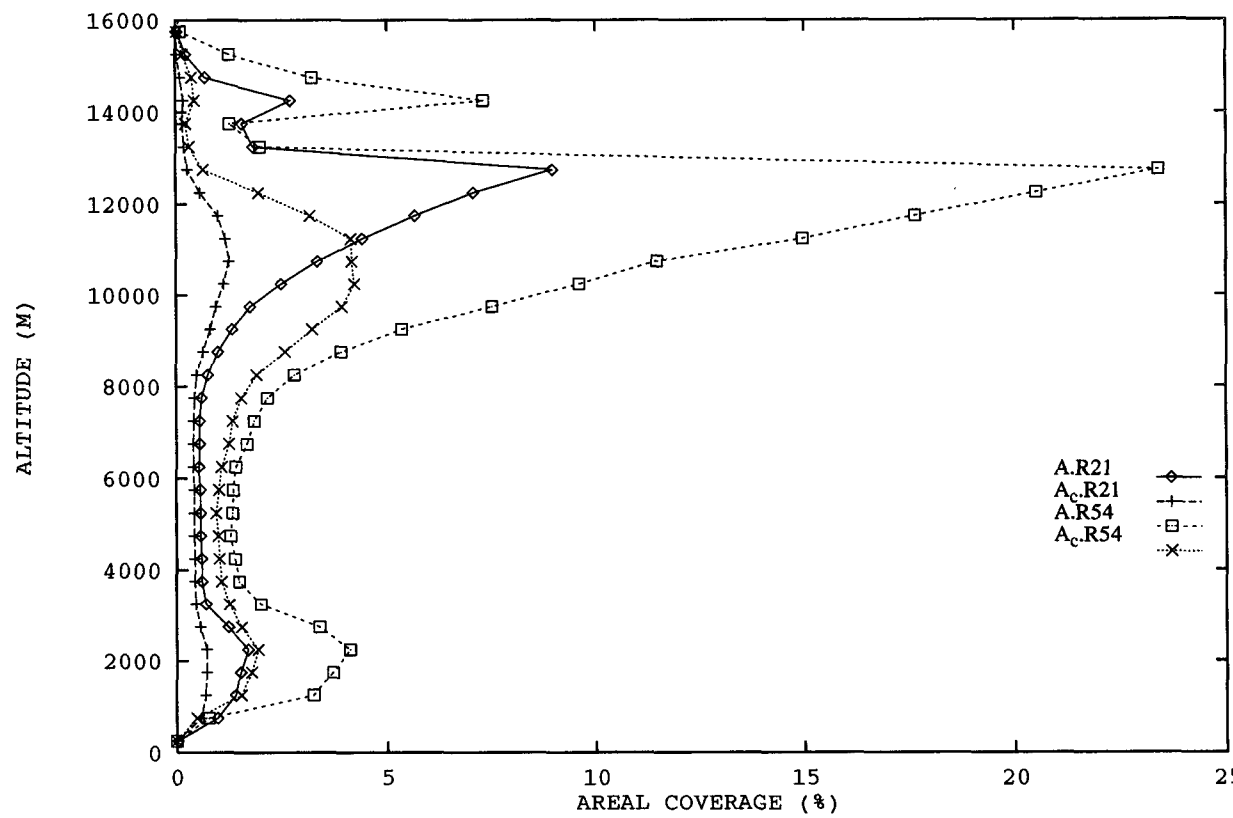


FIG. 9. Cloud cover (for clouds experiencing ascent and convective ascent): time-averaged vertical profiles for R21 ($\sigma \cdot$R21, $\sigma_c \cdot$R21) and R54 ($\sigma \cdot$R54, $\sigma_c \cdot$R54). (Units are in percentages of the total area.)

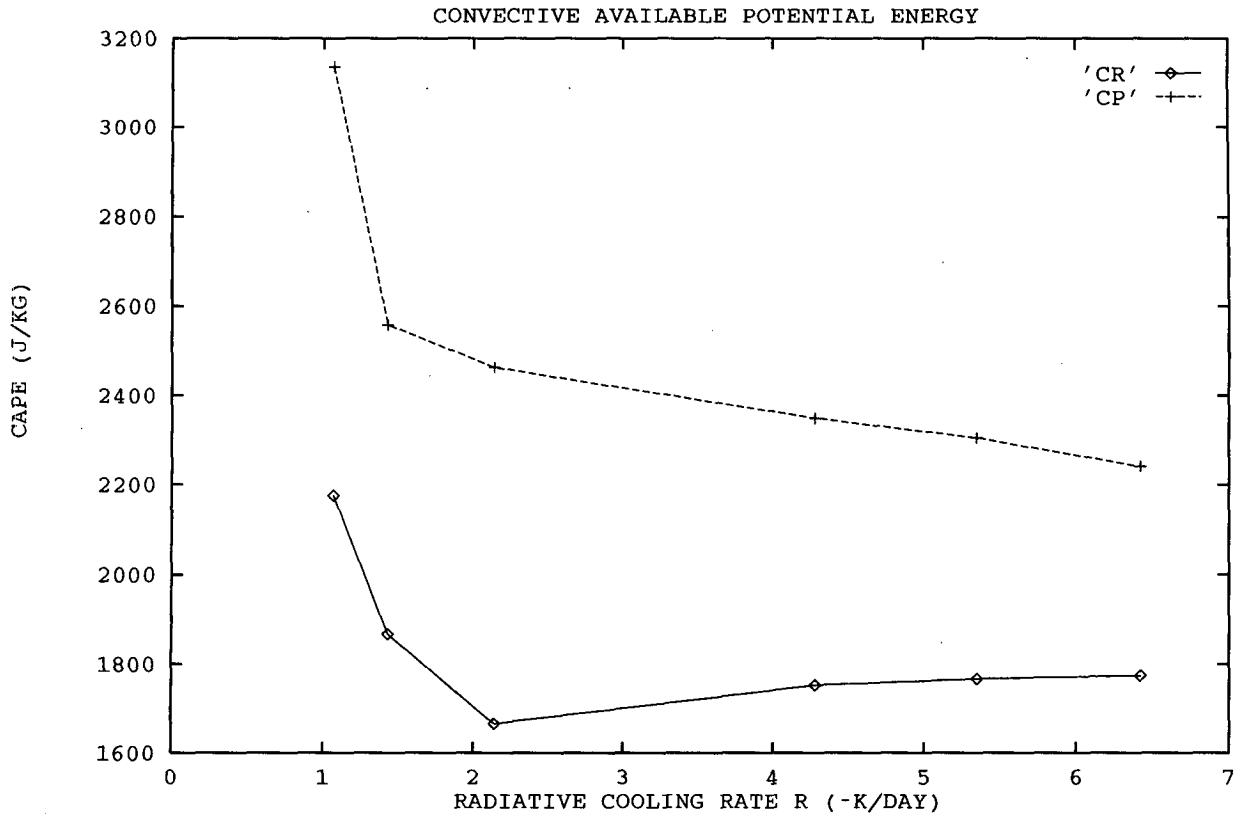


FIG. 10. CAPE of a parcel lifted from 250 m following a reversible ascent (CR) and a pseudoadiabatic ascent (CP): horizontally averaged time means as a function of the radiative cooling rate $R$.

both for pseudoadiabatic (CP) and for reversible (CR) ascent of air from the lowest model level (250 m). These values have been averaged over 2 days of the integration.

For all values of $R$, CP and CR have quite parallel time series (not shown), so if one is not interested in an absolute value of CAPE but rather in its variations with time, one can use either CP or CR. However, their sensitivities to the radiative cooling $R$ are somewhat different. Both CP and CR show a sharp decrease between R11 and R21, then a slow decrease for CP and a very slow increase for CR, for $R$ between $-2.14$ K day$^{-1}$ and $-6.42$ K day$^{-1}$. It is therefore likely that the mean CAPE for an ascent in which some water falls out is nearly constant or slightly decreases with increasing radiative cooling for large values of $R$, and decreases with $R$ for lower values of $R$.

The values of CAPE for the large cooling rate experiments might be underestimated. By fixing the tropopause height, we force a strong inversion between 13 and 14 km, reducing the buoyancy of the parcels above it. However, it is rather complicated to foresee the shape of the sounding and the height of the tropopause at higher cooling rates, since it not only depends on the cooling rate in the troposphere but also on the large-scale motions, distribution of trace gases, and heating in the stratosphere.

## 4. Summary

The net upward mass flux carried by moist convection in statistical equilibrium with the net radiative cooling of the atmosphere is strongly constrained by the requirement that the subsidence warming outside of the active convection balance the radiative cooling:

$$M_{\text{net}} \frac{\partial h_d}{\partial z} = -\dot{Q}_{\text{rad}},$$

where $M_{\text{net}}$ is the net upward mass flux in clouds, $h_d$ is the dry static energy, and $\dot{Q}_{\text{rad}}$ is the rate of radiative cooling. This requirement constrains neither the distribution of the mass flux among individual up- and downdrafts nor the partitioning of the mass flux between fractional areal coverage and upward velocity. Here we have carried out a series of numerical integrations with a "full physics" cloud model integrated on a domain large enough to contain many clouds, and for long enough to achieve statistical equilibrium with an artificially imposed radiative cooling of the atmosphere that is constant up to 13-km altitude, and with surface

fluxes. The results of these integrations show that in the simulations, the convective velocity and buoyancy scales are largely independent of the rate of imposed radiative cooling, so that variations in the latter are absorbed mainly by variations in the fractional areal coverage of convective drafts. In a companion paper, Emanuel and Bister (1996) compare these results to those obtained with a one-dimensional radiative-convective model with parameterized convection, and also explore the dependence of the convective velocity, buoyancy, and areal coverage scales on the vertical distribution of the imposed cooling. A theory of moist convective scales is presented and the predictions are compared to the model results.

*Acknowledgments.* We want to thank K. Droegemeier and M. Xue for providing a copy of the ARPS model as well as for their efficient "consumer service" and helpful advice. The research described herein was supported by Grant ATM-9424201 from the National Science Foundation and by the Center for Global Change Science of the Massachusetts Institute of Technology.

## REFERENCES

Arakawa, A., and W. H. Schubert, 1974: Interaction of a cumulus cloud ensemble with the large-scale environment. Part I. *J. Atmos. Sci.*, **31,** 674–701.

Betts, A. K., 1982: Saturation point analysis of moist convective overturning. *J. Atmos. Sci.*, **39,** 1484–1505.

Deardorff, J. W., 1972: Numerical investigation of neutral and unstable planetary boundary layers. *J. Atmos. Sci.*, **29,** 91–115.

Emanuel, K. A., 1989: Dynamical theories of tropical convection. *Aust. Meteor. Mag.*, **37,** 3–10.

——, 1994: *Atmospheric Convection.* Oxford University Press, 580 pp.

——, 1995: The behavior of a simple hurricane model using a convective scheme based on subcloud-layer entropy equilibrium. *J. Atmos. Sci.*, **52,** 3969–3976.

——, and M. Bister, 1996: Moist convective velocity and buoyancy scales. *J. Atmos. Sci.*, **53,** 3276–3285.

——, J. D. Neelin, and C. S. Bretherton, 1994: On large-scale circulations in convecting atmospheres. *Quart. J. Roy. Meteor. Soc.*, **120,** 1111–1143.

Islam, S., R. L. Bras, and K. A. Emanuel, 1993: Predictability of mesoscale rainfall in the Tropics. *J. Appl. Meteor.*, **32,** 297–310.

Jordan, C. L., 1958: Mean soundings for the West Indies area. *J. Meteor.*, **15,** 91–97.

Kessler, E., 1969: *On the Distribution and Continuity of Water Substance in Atmospheric Circulation. Meteor. Monogr.* No. 32 Amer. Meteor. Soc., 84 pp.

Klemp, J. B., and R. B. Wilhelmson, 1978: The simulation of three-dimensional convective storm dynamics. *J. Atmos. Sci.*, **35,** 1070–1096.

LeMone, M. A., and E. J. Zipser, 1980: Cumulonimbus vertical velocity events in GATE. Part I: Diameter, intensity and mass flux. *J. Atmos. Sci.*, **37,** 2444–2457.

Lilly, D. K., 1960: On the theory of disturbances in a conditionally unstable atmosphere. *Mon. Wea. Rev.*, **88,** 1–17.

Nitta, T., 1975: Observational determination of cloud mass flux distributions. *J. Atmos. Sci.*, **32,** 73–91.

Prandtl, L., 1925: Bericht über Untersuchungen zur ausgebildeten Turbulenz. *Z. Angew. Math. Mech.*, **5,** 136–139.

Raymond, D. J., 1994: Convective processes and tropical atmospheric circulations. *Quart. J. Roy. Meteor. Soc.*, **120,** 1431–1455.

——, 1995: Regulation of moist convection over the west Pacific warm pool. *J. Atmos. Sci.*, **52,** 3945–3959.

Reed, R. J., D. C. Nordquist, and E. E. Recker, 1977: The structure and properties of African wave disturbances as observed during Phase III of GATE. *Mon. Wea. Rev.*, **105,** 317–333.

Renno, N. O., and E. R. Williams, 1995: Quasi-Lagrangian measurements in convective boundary layer plumes. *Mon. Wea. Rev.*, **123,** 2733–2742.

Sui, C. H., K. M. Lau, W. K. Tao, and J. Simpson, 1994: The tropical water and energy cycles in a cumulus ensemble model. Part I: Equilibrium climate. *J. Atmos. Sci.*, **51,** 711–728.

Sun, D.-Z., and R. S. Lindzen, 1993: Distribution of tropical tropospheric water vapor. *J. Atmos. Sci.*, **50,** 1643–1660.

Tao, W.-K., J. Simpson, and S-T. Soong, 1987: Statistical properties of a cloud ensemble: A numerical study. *J. Atmos. Sci.*, **44,** 3175–3187.

Wang, J., and D. A. Randall, 1994: The moist available energy of a conditionally unstable atmosphere. Part II: Further analysis of GATE data. *J. Atmos. Sci.*, **51,** 703–710.

Williams, E., and N. Renno, 1993: An analysis of the conditional instability of the tropical atmosphere. *Mon. Wea. Rev.*, **121,** 21–36.

Xu, K.-M., 1995: Partitioning mass, heat, and moisture budgets of explicitly simulated cumulus ensembles into convective and stratiform components. *J. Atmos. Sci.*, **52,** 551–573.

——, and K. A. Emanuel, 1989: Is the tropical atmosphere conditionally unstable? *Mon. Wea. Rev.*, **117,** 1471–1479.

——, A. Arakawa, and S. Krueger, 1992: The macroscopic behavior of cumulus ensembles simulated by a cumulus ensemble model. *J. Atmos. Sci.*, **49,** 2402–2420.

Xue, M., K. K. Droegemeier, V. Wong, A. Shapiro, and K. Brewster, 1993: *Advanced Regional Prediction System, Version 3.1. User's Guide,* 186 pp. [Available from the Center for Analysis and Prediction of Storms, University of Oklahoma, Norman, OK 73019.]

Zipser, E. J., and M. A. LeMone, 1980: Cumulonimbus vertical velocity events in GATE. Part II: Synthesis and model core structure. *J. Atmos. Sci.*, **37,** 2458–2469.